

Control System to Balance Internal Currents of a Multilevel Current-Source Inverter

Pablo Cossutta^{ID}, Member, IEEE, Miguel Pablo Aguirre, Senior Member, IEEE, Mathias Angelico Engelhardt, Member, IEEE, and María Inés Valla^{ID}, Fellow, IEEE

Abstract—Multilevel current-source inverters have proved to be a high-performance option for industrial applications due to reliability, fault-tolerant capabilities, quasi soft switching, and the use of lower filter capacitor values. One of its major challenges is to balance the internal currents that feed each module. Imbalances could be caused by manufacturing deviations of the reactive components, temperature drift or aging, nonlinear loads, and modulation errors, among others. Using the well-known phase-shift carrier sinusoidal pulse width modulation, a slight change in the amplitude of the carrier signals produces a variation in the average value of the internal currents. In this paper, we introduce a control strategy to balance the current of the inductors and its implementation in a prototype. Simulation and experimental results at different operating conditions show a robust behavior of the control system along with a low distortion in the output voltages and currents of the converter.

Index Terms—Field-programmable gate array (FPGA) control, inductor current balance, multilevel current-source inverter (MCSI).

I. INTRODUCTION

OVER the past years, multilevel power converters have been used in several applications such as battery chargers [1], power factor correctors [2] and active filters [3], motor control [4]–[6], and interface with alternative energy sources [7]–[9], among many others [10]. They can be implemented both as a multilevel voltage-source inverter (MVASI) or multilevel current-source inverter (MCSI).

MCSIs particularly offer a great number of advantages such as a fast dynamic response, fault-tolerant capabilities, and the

reduction of high-frequency electrical disturbances in the load. Furthermore, they have less current stress in the switches and an increased medium time between failures because of the higher reliability of inductors compared to MVSI capacitors[11]–[13]. Their main disadvantages are the required reverse voltage-blocking capabilities of the switches and the size and weight of the internal inductors. These disadvantages could be partially solved by using widebandgap devices such as SiC and GaN that allow us to increase the frequency without affecting efficiency [14]–[16].

The topology called “single-rating-inductor MCSI” in [17] consists of n identical current-source inverter (CSI) modules. Each module is composed of two balance inductors and six switches that have reverse voltage-blocking characteristics. One of the modulation techniques commonly used in these kinds of converters is the well-known phase-shift carrier sinusoidal pulse width modulation (PSC-SPWM) [18], [19], which is based on the comparison of three sinusoidal references with a triangular carrier. Each module applies the SPWM technique taking into account that the phase of the carrier must be equally shifted by $\frac{360}{n}$ degrees.

The MCSI presents $2n + 1$ current levels since each module has the capability of injecting $\pm \frac{1}{n}$ of the main dc current. The whole operation of the MCSI assumes that each module has the same current value. However, unmatched components, unequal ON-state characteristics of the semiconductor devices, modulation errors, and nonlinear loads could cause an imbalance in these currents, so a balancing method must be implemented.

Even though the issue related to the voltage imbalance in the capacitors of different MVSI topologies has been widely studied in the literature [20]–[24], only a few techniques applied to the MCSI topology could be found [25]–[28].

The methods proposed in [25] and [26] deal with a five-level MCSI, and they are not easily extended to more levels. In [25], the balance of the internal currents is achieved by choosing the proper redundant vector in the space vector modulation. In [26], a complex logic is used to modify the PSC-SPWM in order to balance the current of the two modules. Extra hardware is introduced in [27] to balance the currents in a five-level single-phase MCSI. Two methods based on the PSC-SPWM were proposed in [28]. A slight change either in the amplitude or the phase of the triangular carriers causes a change in the internal currents that could be used to generate a balanced operating point. The controller action slightly affects the output current total harmonic distortion (THD) without affecting the switching losses.

This work was supported by the Instituto Tecnológico de Buenos Aires, Universidad Nacional de La Plata, Consejo Nacional de Investigaciones Científicas y Técnicas, and Agencia Nacional de Promoción de Ciencia y Tecnología through Grant PICT-2015-3040, Grant PIP-2015-0100496, and Grant UNLP-11/217. (*Corresponding author: Pablo Cossutta.*)

P. Cossutta, M. P. Aguirre, and M. A. Engelhardt are with the Centro de Investigación y Desarrollo en Electrónica Industrial, Instituto Tecnológico de Buenos Aires, C1106ACD Buenos Aires, Argentina (e-mail: pcossutt@itba.edu.ar; maguir@itba.edu.ar; mangelic@itba.edu.ar).

M. I. Valla is with the Instituto de Investigaciones en Electrónica, Control y Procesamiento de Señales (LEICI, CONICET-UNLP) Facultad de Ingeniería, National University of La Plata, 1900 La Plata, Argentina (e-mail: m.i.valla@ieee.org).

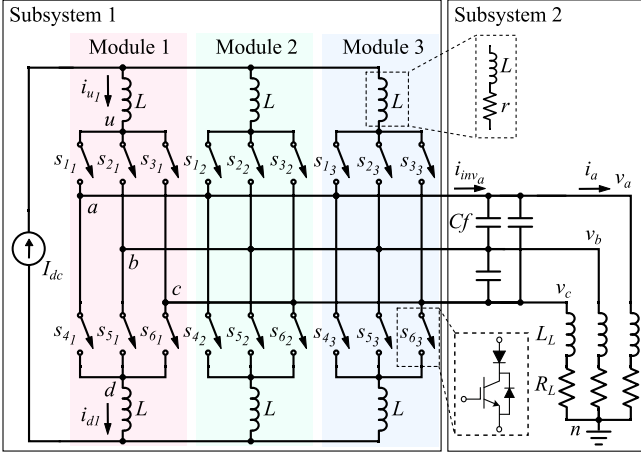


Fig. 1. MCSI topology.

In this paper, the mathematical model of the MCSI and a current balance control algorithm is developed. A new version of the algorithm proposed in [28] is presented, analyzed, and verified with an MCSI prototype under different experimental conditions. The proposed controller is based on controlling the average value between the upper and lower currents of each CSI module. The controller, along with the SPWM, is implemented in a field-programmable gate array (FPGA) as in [29], allowing high-speed data processing, variable bit accuracy, fault-tolerant architectures, and easily scalable design [30], [31]. In addition to these qualities, one of the most powerful advantages of an FPGA is the ability to compute all the converter control blocks in parallel, saving time and increasing reliability. In order to be scalable and comparable to the experimental results, simulation models in this paper consider the internal logic timing, the switches behavior, the parameters of the experimental setup, and the saturation limits of the actual control system.

In detail, this paper is organized as follows. In Section II, the system is described and its mathematical model is obtained. Then, the modulator and proposed controller are shown. Section III presents and analyzes the simulation results. Experimental results are shown in Section IV. Finally, in Section V, some conclusions are drawn.

II. SYSTEM DESCRIPTION

The system is composed of an MCSI, a dc current source, custom acquisition boards used to measure the internal currents of the MCSI, an FPGA, filtering capacitors, and the load.

A. MCSI Topology

Fig. 1 shows the schematics of the MCSI. It consists of three CSI modules in parallel with a maximum of seven different output current levels. Two inductors are required in each module to balance its current value. All the balance inductors should be identical and should carry the same average current, simplifying the design of the inverter. Each module is composed of six reverse blocking switches that could be implemented

with integrated-gate commutated thyristors, reverse blocking insulated-gate bipolar transistors, or insulated-gate bipolar transistors with a series diode to block the reverse current and voltage, among others. In order to filter and improve the current and voltage waveforms at the load, a three-phase capacitor of a low capacitance value is placed at the output of the MCSI.

B. Mathematical Model

At any given time, each module of the multilevel inverter must grant a current path, so one upper switch and one lower switch must be conducting. Furthermore, only one of the upper and lower devices must be conducting to ensure that the injected current of the inverter is defined only by the dc current source and the state of the switches. These restrictions can be stated as follows:

$$s_{1_y} + s_{2_y} + s_{3_y} = s_{4_y} + s_{5_y} + s_{6_y} = 1, \quad y \in \{1, 2, 3\} \quad (1)$$

where the last subindex y is the module number, with $s_{1,6_y} = 1$ when the switch is conducting and 0 otherwise. The proposed topology can be modeled as two interconnected subsystems: one involving the MCSI with its current source and the other composed of filtering capacitors and a load, which are shown in Fig. 1 as Subsystem 1 and Subsystem 2. Both models have six state variables with the output of the first model connected to the input of the second one and vice versa. Applying the Kirchhoff's laws on the topology and rearranging the equations, the state-space model of the MCSI is obtained

$$\begin{bmatrix} \dot{i}_{u_1} \\ \dot{i}_{u_2} \\ \dot{i}_{u_3} \end{bmatrix} = \frac{1}{3L} \Gamma \begin{bmatrix} v_{un_1} \\ v_{un_2} \\ v_{un_3} \end{bmatrix} - \frac{r}{L} \begin{bmatrix} i_{u_1} \\ i_{u_2} \\ i_{u_3} \end{bmatrix} + \frac{r}{3L} \begin{bmatrix} 1 \\ 1 \\ 1 \end{bmatrix} I_{dc} \quad (2)$$

$$\begin{bmatrix} \dot{i}_{d_1} \\ \dot{i}_{d_2} \\ \dot{i}_{d_3} \end{bmatrix} = \frac{1}{3L} \Gamma \begin{bmatrix} v_{nd_1} \\ v_{nd_2} \\ v_{nd_3} \end{bmatrix} - \frac{r}{L} \begin{bmatrix} i_{d_1} \\ i_{d_2} \\ i_{d_3} \end{bmatrix} + \frac{r}{3L} \begin{bmatrix} 1 \\ 1 \\ 1 \end{bmatrix} I_{dc} \quad (2)$$

where L is the self-inductance of each module with an internal resistance r , the matrix Γ is

$$\Gamma = \begin{bmatrix} -2 & 1 & 1 \\ 1 & -2 & 1 \\ 1 & 1 & -2 \end{bmatrix} \quad (3)$$

and

$$\begin{bmatrix} v_{un_1} \\ v_{un_2} \\ v_{un_3} \end{bmatrix} = \begin{bmatrix} s_{1_1} & s_{2_1} & s_{3_1} \\ s_{1_2} & s_{2_2} & s_{3_2} \\ s_{1_3} & s_{2_3} & s_{3_3} \end{bmatrix} \begin{bmatrix} v_a \\ v_b \\ v_c \end{bmatrix}$$

$$\begin{bmatrix} v_{nd_1} \\ v_{nd_2} \\ v_{nd_3} \end{bmatrix} = - \begin{bmatrix} s_{4_1} & s_{5_1} & s_{6_1} \\ s_{4_2} & s_{5_2} & s_{6_2} \\ s_{4_3} & s_{5_3} & s_{6_3} \end{bmatrix} \begin{bmatrix} v_a \\ v_b \\ v_c \end{bmatrix} \quad (4)$$

in which s_{x_y} are the state of the switches, x is the switch number, and y is the module number. The output current of the inverter

is stated as follows:

$$\begin{bmatrix} i_{\text{inv}_a} \\ i_{\text{inv}_b} \\ i_{\text{inv}_c} \end{bmatrix} = \begin{bmatrix} s_{1_1} & s_{1_2} & s_{1_3} \\ s_{2_1} & s_{2_2} & s_{2_3} \\ s_{3_1} & s_{3_2} & s_{3_3} \end{bmatrix} \begin{bmatrix} i_{u_1} \\ i_{u_2} \\ i_{u_3} \end{bmatrix} - \begin{bmatrix} s_{4_1} & s_{4_2} & s_{4_3} \\ s_{5_1} & s_{5_2} & s_{5_3} \\ s_{6_1} & s_{6_2} & s_{6_3} \end{bmatrix} \begin{bmatrix} i_{d_1} \\ i_{d_2} \\ i_{d_3} \end{bmatrix}. \quad (5)$$

The second subsystem that includes the load and the filter capacitors is modeled by

$$\begin{bmatrix} \dot{v}_a \\ \dot{v}_b \\ \dot{v}_c \\ \dot{i}_a \\ \dot{i}_b \\ \dot{i}_c \end{bmatrix} = \begin{bmatrix} 0 & 0 & 0 & a & 0 & 0 \\ 0 & 0 & 0 & 0 & a & 0 \\ 0 & 0 & 0 & 0 & 0 & a \\ b & 0 & 0 & c & 0 & 0 \\ 0 & b & 0 & 0 & c & 0 \\ 0 & 0 & b & 0 & 0 & c \end{bmatrix} \begin{bmatrix} v_a \\ v_b \\ v_c \\ i_a \\ i_b \\ i_c \end{bmatrix} - a \begin{bmatrix} i_{\text{inv}_a} \\ i_{\text{inv}_b} \\ i_{\text{inv}_c} \\ 0 \\ 0 \\ 0 \end{bmatrix}$$

$$a = -\frac{1}{3C_F}, \quad b = \frac{1}{L_L}, \quad c = -\frac{R_L}{L_L} \quad (6)$$

where C_F represents the filter capacitance, R_L the load resistance, and L_L load inductance. The interconnection between the two subsystems can be seen in (4) and (5). As shown in (2), the dynamics of the upper and lower currents, i_{u_y} and i_{d_y} , are different because they depend on the state of the switches and load voltages. Thus, a classic controller would have taken into account the values of the six internal currents in order to balance them. However, balancing the average value between the upper and lower currents for each module is a simpler approach that produces similar results. The average currents are defined by

$$\bar{i}_y = \frac{i_{u_y} + i_{d_y}}{2}, \quad y \in \{1, 2, 3\}. \quad (7)$$

As this paper is focused on balancing the average currents, the resulting dynamics to control can be expressed as

$$\begin{bmatrix} \dot{\bar{i}}_1 \\ \dot{\bar{i}}_2 \\ \dot{\bar{i}}_3 \end{bmatrix} = \frac{1}{6L} \begin{bmatrix} -2 & 1 & 1 \\ 1 & -2 & 1 \\ 1 & 1 & -2 \end{bmatrix} \begin{bmatrix} v_1 \\ v_2 \\ v_3 \end{bmatrix} - \frac{r}{L} \begin{bmatrix} \bar{i}_1 \\ \bar{i}_2 \\ \bar{i}_3 \end{bmatrix} + \frac{r}{3L} \begin{bmatrix} 1 \\ 1 \\ 1 \end{bmatrix} I_{dc} \quad (8)$$

where the equivalent voltages of each module, v_1 , v_2 , and v_3 , are defined by

$$\begin{bmatrix} v_1 \\ v_2 \\ v_3 \end{bmatrix} = \begin{bmatrix} v_{un_1} \\ v_{un_2} \\ v_{un_3} \end{bmatrix} + \begin{bmatrix} v_{nd_1} \\ v_{nd_2} \\ v_{nd_3} \end{bmatrix}. \quad (9)$$

Since $v_{1,2,3}$, in (8), depend on the state of the switches, a variation in the modulation algorithm could be used to produce a change in the average current of all the modules.

C. Modulation

The modulation of the MCSI is performed applying the PSC-SPWM. It is based on comparing the reference sinusoidal signals with three equally phase-shifted triangular carriers [18]. A block

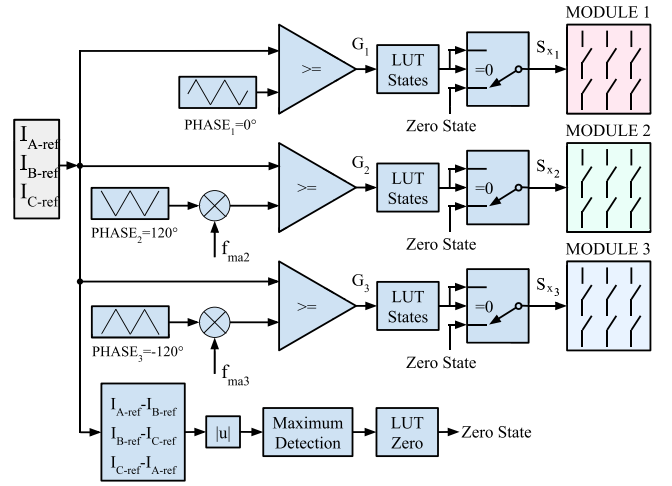


Fig. 2. Modulation scheme.

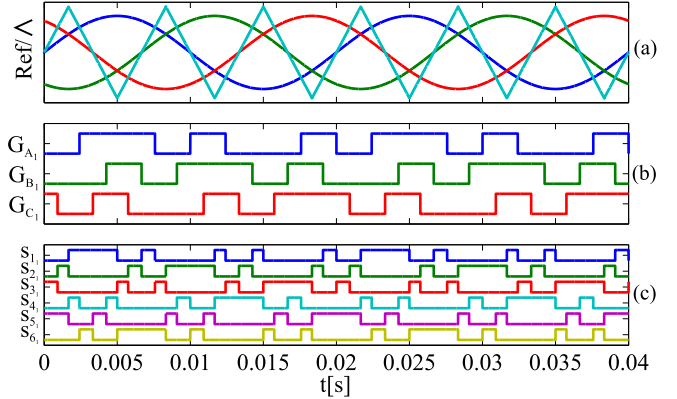


Fig. 3. SPWM detail of one module.

diagram of the modulation stage is presented in Fig. 2, where $f_{ma2,3}$ are the outputs of the controller, which is described in the next section. They are equal to 1 when the control is disabled. The implementation of this modulation in a CSI is not as simple as in a VSI, since it requires more logic manipulation to generate the desired current levels at the output while ensuring a current path in all the inductors. Since the modulation algorithm is similar for each module, the modulation scheme of the first one is used as an example. The different signals of the modulation process are shown in Fig. 3. First, the current references of the MCSI, $I_{A-\text{ref}}$, $I_{B-\text{ref}}$, and $I_{C-\text{ref}}$, are compared with the triangular carrier as depicted in Fig. 3(a). The standard VSI SPWM signals G_{A_1} , G_{B_1} , and G_{C_1} , shown in Fig. 3(b), are generated by the comparators. They are used as inputs of the lookup table states (LUT States), as shown in the top part of Fig. 2. The LUT States, shown in Table I, are used to transform the active vectors of a VSI, generated by the SPWM, into equivalent active vectors of a CSI. Zero vectors are considered separately. Since each module can produce a zero current state by turning ON both switches in any of its three legs, the CSI has one extra zero state than the VSI. This extra redundancy could be used to reduce the commutation frequency, reduce the

TABLE I
LUT STATES OF MODULE x

Input			Output					
G_{A_x}	G_{B_x}	G_{C_x}	s_{1_x}	s_{2_x}	s_{3_x}	s_{4_x}	s_{5_x}	s_{6_x}
0	0	0	0	0	0	0	0	0
0	0	1	0	0	1	0	1	0
0	1	0	0	1	0	1	0	0
0	1	1	0	0	1	1	0	0
1	0	0	1	0	0	0	0	1
1	0	1	1	0	0	0	1	0
1	1	0	0	1	0	0	0	1
1	1	1	0	0	0	0	0	0

TABLE II
LUT ZERO, $x = 1, 2, 3$

Maximum value	Output					
	s_{1_x}	s_{2_x}	s_{3_x}	s_{4_x}	s_{5_x}	s_{6_x}
$ I_A - I_B - \text{ref} $	1	0	0	1	0	0
$ I_B - I_C - \text{ref} $	0	1	0	0	1	0
$ I_C - I_A - \text{ref} $	0	0	1	0	0	1

power dissipation, and increase the efficiency. To select the zero state that meets these goals, first three current differences are calculated and the one that gets the maximum absolute value is related to the optimum zero state. Another lookup table (LUT Zero), which is shown in Table II, holds the zero states. Both the output of the LUT States and the LUT Zero are fed into a multiplexer. The outputs of the multiplexer, $s_{1_1}, s_{2_1}, s_{3_1}, s_{4_1}, s_{5_1}$, and s_{6_1} , are shown in Fig. 3(c).

D. Controller

One of the major drawbacks of the multilevel topologies is that the average currents of each module, $\bar{i}_{1,2,3}$, may have different mean values. This could be caused by nonlinear loads, imperfections of the modulation algorithm, unequal ON-state characteristics of the semiconductor devices, and component variations. In this section, a control algorithm to balance these currents is presented. The control algorithm is based on the one proposed in [28], which uses slight changes of the PSC-SPWM carriers. In [28], the amplitudes of the triangular carriers in the modules 2 and 3 are modified in order to balance the internal currents. The objective of this controller is just to balance only the average between the upper, i_{u_y} , and lower, i_{d_y} , currents of each module. The upper and lower currents of one module, along with their average value, are depicted in Fig. 4. It can be noticed that the current waveforms have two different parts: a flat zone and a ripple zone. The different mean values can be clearly recognized since the constant flat zone of each current is at a different level and depends on the relative phase and the amplitude relation between the carriers and the reference signals, m_a . The average current, defined in (7), has a lower ripple and its mean value could be obtained with a low-pass filter. From (4), it can be deduced that a change in the SPWM

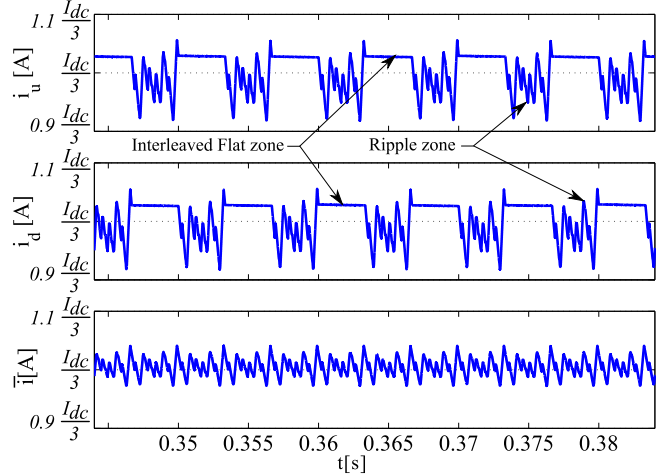


Fig. 4. From top to bottom: First trace: i_u , second trace i_d , and third trace: \bar{i} , average current of one module.

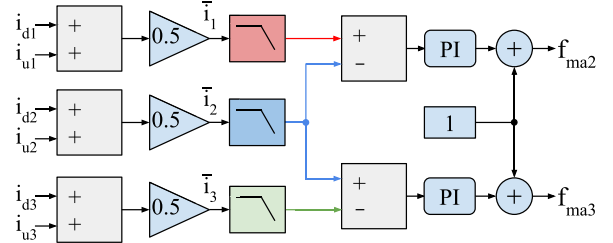


Fig. 5. Proposed current balance controller.

carriers causes a change in the switch signals and, hence, a change in the upper and lower voltages seen by each of the modules $v_{un1}, v_{un2}, v_{un3}, v_{nd1}, v_{nd2}$, and v_{nd3} . Taking into account (9), these voltages are the inputs of the dynamic expressed in (8), which is the state-space representation of the average currents, which must be controlled. The overall control algorithm is depicted in Fig. 5. The controller is implemented with two simple proportional–integral (PI) controllers. A change in the amplitude of the carrier that is used in the second module produces a variation of \bar{i}_1 and \bar{i}_2 , while changing the amplitude of the third carrier produces a variation of \bar{i}_2 and \bar{i}_3 . Considering this behavior, the error signal for the first PI is implemented by the difference between \bar{i}_1 and \bar{i}_2 , while the error signal for the second one is done by the difference between \bar{i}_2 and \bar{i}_3 . The low-pass filter is needed because the main objective is to control the average current on the inductors of the converter and the commutation frequency must be rejected for this purpose. Since the aim of the controller is to introduce a slight change in the carrier amplitudes, a saturation of $\pm 6\%$ of the maximum m_a is applied to the output of the PI controllers in order to limit their action and its effect over the SPWM signals. Then, the PI outputs are added to 1 to create a scale factor for the amplitude of both carriers. Both f_{ma2} and f_{ma3} signals are fed into the modulation scheme shown in Fig. 2. The frequency of the triangular carriers is not affected as the controller changes only their amplitudes. Therefore, there is no change on the

TABLE III
SYSTEM PARAMETERS

Parameter	Value
I_{dc}	10 A
Line frequency	50 Hz
Balance inductors (L, r)	80 mH, 0.75 Ω
Capacitor Filter (C_f)	4.7 μF
Frequency Modulation Index (m_f)	21
Carrier frequency	1050 Hz
Load (R_L, L_L)	16 Ω, 9 mH

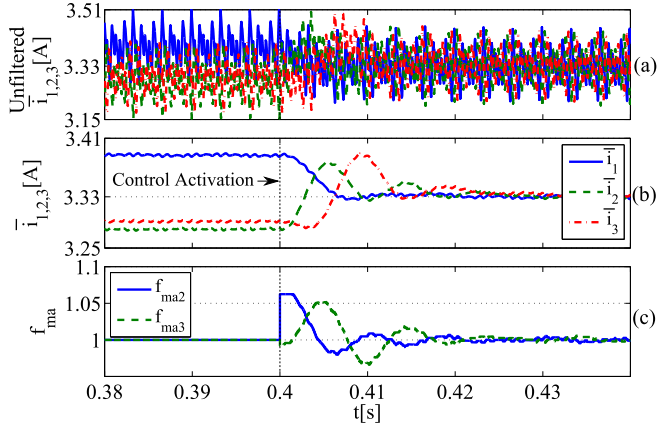


Fig. 6. Simulation of the proposed controller—Internal average currents $\bar{i}_{1,2,3}$, filtered and unfiltered, and control output signals f_{ma2} and f_{ma3} .

average commutation frequency, and hence, switching losses are not affected.

III. SIMULATION RESULTS

Extensive simulations were performed using the SimPowerSystem toolbox from MATLAB/Simulink down to switch level. The parameters used in the simulations and experiments are shown in Table III. The chosen bandwidth for the low-pass digital filter, which is used to smooth the average of the upper and lower currents of each module, is 155 Hz and the modulation index ma is 0.9. The controller is designed in discrete time with a sampling time $T_s = 1 \mu\text{s}$.

Fig. 6 shows the response of the system before and after the controller is enabled. With the controller disabled, the scale factors remain at 1 and the internal currents have a difference of 100 mA. At time $t = 0.4$ s, the controller is enabled and the average currents converge to approximately 3.33 A in less than 30 ms. The filtered average currents $\bar{i}_{1,2,3}$ shown in Fig. 6(b) are used to feed the digital controllers. The output control signals that modify the amplitude of the triangular carriers in the modulation block are depicted in Fig. 6(c).

Fig. 7 shows the output variables of the system under examination. The output current i_a , shown in the third trace, is the inverter output of the phase a , i_{inv_a} , filtered by the output capacitors. The output variables of the system remain practically unchanged when the control is enabled. The output line voltage v_{ab} , shown in the second trace, is affected mainly by the fifth and higher order harmonics.

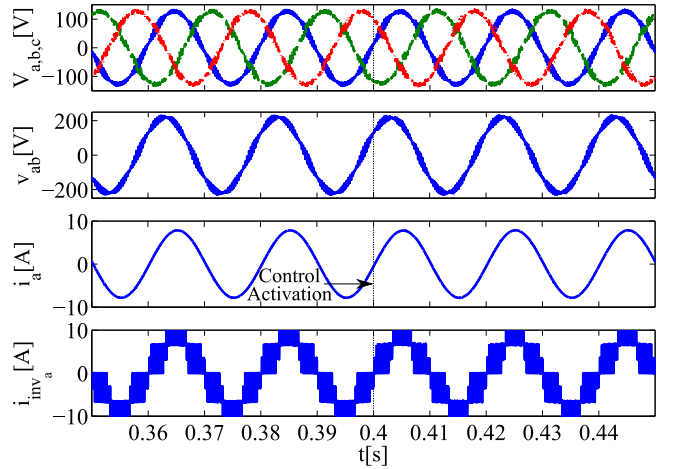


Fig. 7. Simulation of the proposed controller. Phase voltages $v_{a,b,c}$, line voltage v_{ab} , current i_a , and the unfiltered output of the inverter i_{inv_a} .

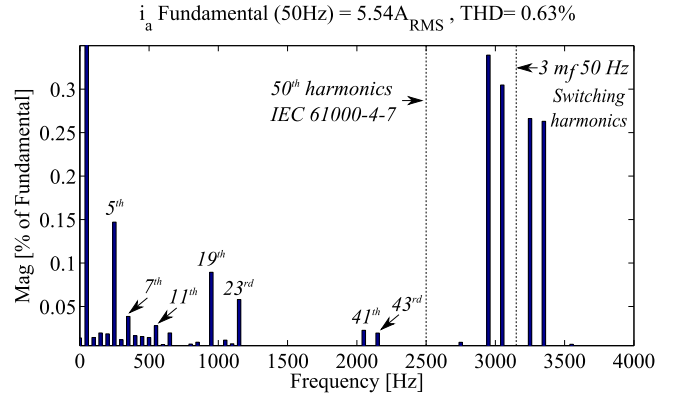


Fig. 8. THD of the simulated output current i_a with the controller enabled.

As shown in Fig. 8, the output current i_a presents low harmonic distortion and a THD of 0.63% even when the controller is enabled. The main difference with the theoretical spectrum of a discrete-time SPWM modulator is the presence of low-order harmonics, less than 0.025% of the fundamental current. These low-order harmonics are caused by the effects of the quantization in the modulation and control algorithm. The main components of the i_a spectrum are also caused by the fifth harmonic and the switching harmonics. Since the MCSI consists of three identical modules to produce seven levels in the output current, the switching components are three times the commutation frequency of the switches or $3 m_f 50$ Hz, where m_f is the frequency modulation index. Hence, the harmonics corresponding to the switching frequency are centered at 3150 Hz.

Fig. 9 shows the response of the system under a step down in m_a . At time $t = 0.46$ s, it is changed from 0.9 to 0.5 and the controller is able to balance the internal currents with a settling time of less than 40 ms. The change of m_a causes a reduction in the number of levels that the MCSI outputs. It also produces an instant change on the current and voltage at the load. The ripple introduced in the internal average currents during the transient is less than 2.5%.

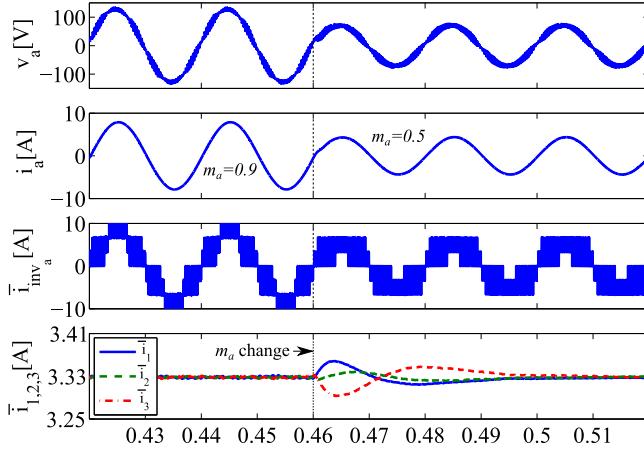


Fig. 9. Simulation of the proposed controller with $m_a = 0.5$, phase voltage v_a , phase current i_a , unfiltered output of the inverter i_{inv_a} , and internal average currents $\bar{i}_{1,2,3}$

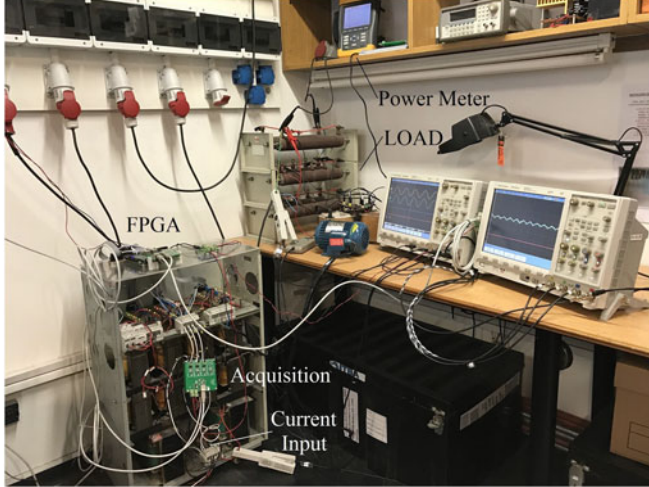


Fig. 10. Experimental setup.

IV. EXPERIMENTAL RESULTS

A custom acquisition system was designed and developed in order to measure the internal currents of the MCSI. The current is sensed using the ACS714 Hall effect sensor, a four-channel 12-bit analog-to-digital converter with a serial peripheral interface capable of sampling up to 1 MSps, digital isolators, and LVDS converters to improve the CMRR of the communication with the FPGA [32]. Control algorithms along with the SPWM and support logic are implemented on a Xilinx FPGA, Xilinx Zynq-7000 AP SoC XC7Z020. It uses 1763 lookup tables, four digital signal processing blocks used as multipliers in PIs, and five block random access memory, which represents less than 4% of the overall capacity. The experimental setup, which is composed of an MCSI, a dc current source, different types of loads, a power meter, acquisition, and FPGA boards, is shown in Fig. 10. The parameters of the system are the same as used in the previous section.

The internal filtered currents of each module $\bar{i}_{1,2,3}$ are shown in Fig. 11 prior and post controller activation. The ripple is

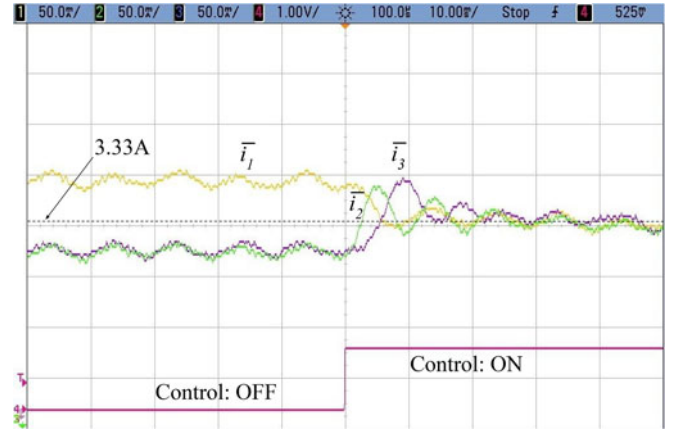


Fig. 11. Internal average currents with and without control. Upper traces: internal average currents $\bar{i}_{1,2,3}$ at a scale of 50 mA/div. Bottom trace: control enable signal.

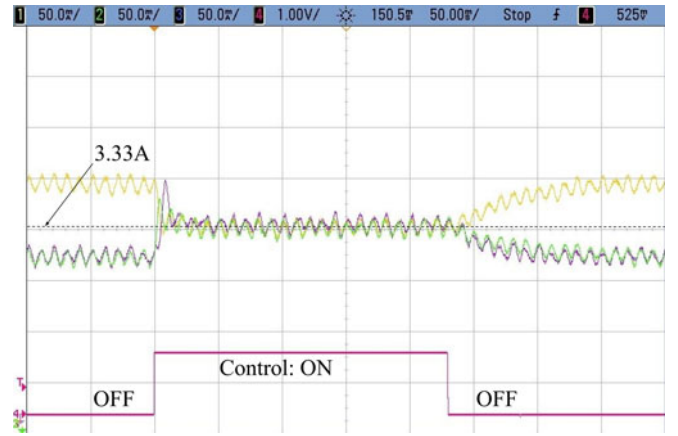


Fig. 12. Step on control activation. Internal average currents with and without control. Upper traces: internal average currents $\bar{i}_{1,2,3}$ at a scale of 50 mA/div. Bottom trace: control enable signal.

mainly caused by the current source that supplies the MCSI, which has a ripple of approximately 2% and the zero state selection of the modulator. When the controller is disabled, the internal currents have a difference of 80 mA. After the controller is enabled, the internal currents of each module show the desired response converging to 3.33 A in less than 50 ms.

In Fig. 12, the controller is enabled and disabled again after 230 ms. After being enabled, the currents of each module converge to the same value, and when the control is disabled, the currents return to their original value with a longer settling time. The longer settling time is caused by the open-loop response of the system, which depends only on the topology and the system parameters.

Fig. 13 shows the voltage v_a , current i_a , and input current i_{dc} along with the control enable signal. Both v_a and i_a present a low distortion due to the multilevel capabilities of the inverter along with its high equivalent commutation frequency. There are no noticeable differences in the waveforms after the control is enabled.

The variation of the scale factors, $f_{ma2,3}$, after the controller is enabled is shown in Fig. 14. They introduce a slight change

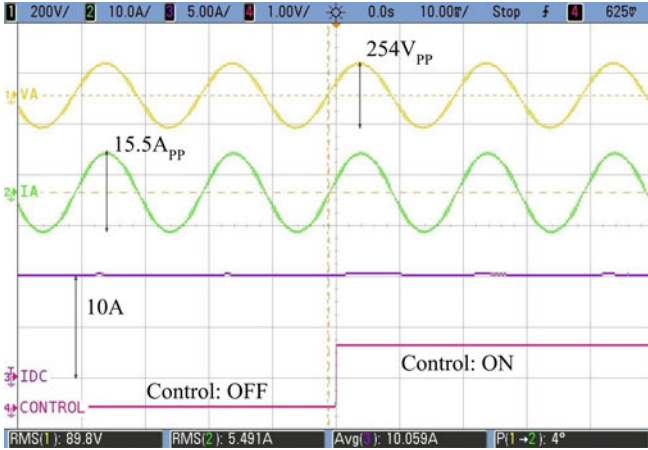


Fig. 13. Traces from top to bottom. First: output voltage v_a [V] at a scale of 200 V/div. Second: output current i_a [A] at a scale of 10 A/div. Third: input current I_{dc} [A] at a scale of 5 A/div. Fourth: control enable signal.

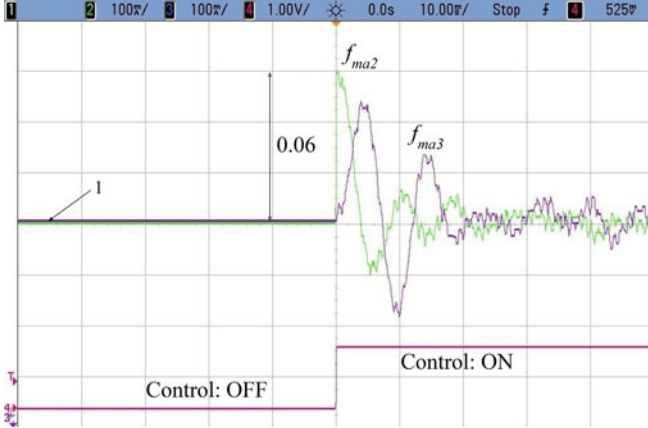


Fig. 14. Controller output signals with and without control. Upper traces: f_{ma2} and f_{ma3} at a scale of 0.02/div. Bottom trace: control enable signal.

in the triangular carriers to perform the balancing of the internal currents. A good correlation between simulation and experimental results is observed.

The spectrum of the output waveforms v_a and i_a is depicted in Figs. 15 and 16, respectively. The first 50 harmonics were measured using a Fluke 435 Series II Power Quality and Energy Analyzer, according to the IEC 61000-4-7 standard. The main differences with the simulation are the presence of the third harmonic and an increment of 0.1% in most of the harmonics. The third harmonic is introduced mainly by the ripple of the dc current source. The power differences are due to delays introduced by the semiconductor switches, accuracy and resolution of the power meter, and small errors introduced by the FPGA implementation. The THD of the current is 0.3% when the controller is disabled and increases to 0.4% when enabled. The same behavior is observed for the voltage THD that gets increased to 0.6% when the controller is enabled. Results are very promising

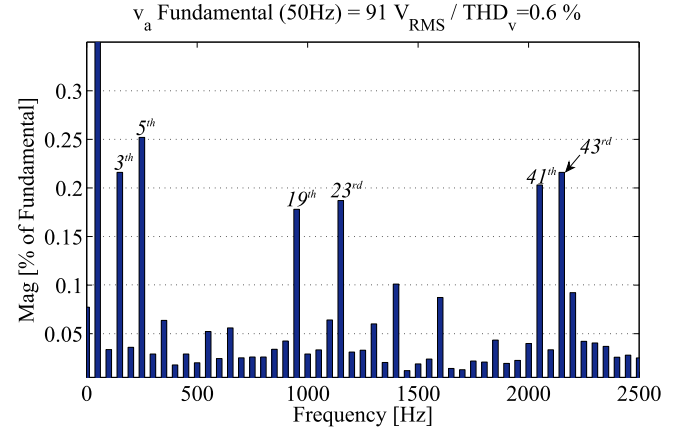


Fig. 15. THD measurement of output voltage v_a with control enabled.

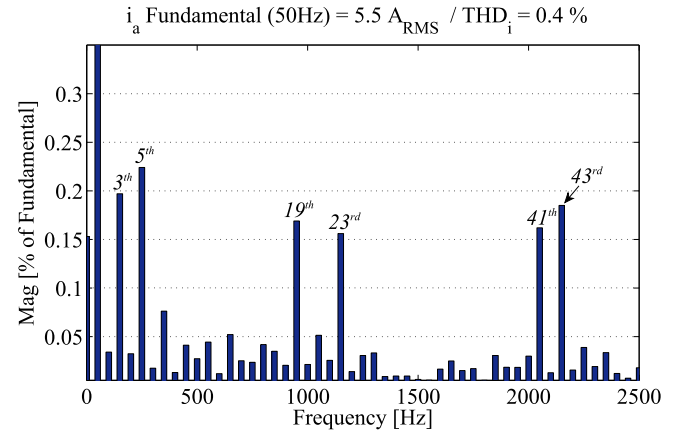


Fig. 16. THD measurement of output current i_a with control enabled.

since, even when the controller is activated, THD values are below the 3% established by the IEC 61000-4-7 and the IEEE Standard 519.

V. CONCLUSION

A control technique to ensure the balance of the internal currents on an MCSI was presented. Although the implementation needs the measurement of the internal currents, it requires little computational effort, and, hence a small area on an FPGA. It also introduces a minimal distortion to the SPWM signals without affecting the switching losses and increasing less than 0.1% the THD at the output of the inverter. The controller was designed, evaluated through simulations, and implemented on a prototype of a seven-level MCSI. Simulation and experimental results showed an excellent behavior. This solution can be easily expanded by adding only a PI controller for each additional module.

The proposed controller is suitable for industrial converters as it can withstand disturbances and imbalances of the components without affecting the internal currents of the MCSI.

REFERENCES

- [1] J. I. Y. Ota, T. Sato, and H. Akagi, "Enhancement of performance, availability, and flexibility of a battery energy storage system based on a modular multilevel cascaded converter (MMCC-SSBC)," *IEEE Trans. Power Electron.*, vol. 31, no. 4, pp. 2791–2799, Apr. 2016, DOI: [10.1109/TPEL.2015.2450757](https://doi.org/10.1109/TPEL.2015.2450757).
- [2] D. F. Cortez and I. Barbi, "A three-phase multilevel hybrid switched-capacitor PWM PFC rectifier for high-voltage-gain applications," *IEEE Trans. Power Electron.*, vol. 31, no. 5, pp. 3495–3505, May 2016, DOI: [10.1109/TPEL.2015.2467210](https://doi.org/10.1109/TPEL.2015.2467210).
- [3] R. Mo and H. Li, "Hybrid energy storage system with active filter function for shipboard MVDC system applications based on isolated modular multilevel dc/dc converter," *IEEE J. Emerg. Sel. Topics Power Electron.*, vol. 5, no. 1, pp. 79–87, Mar. 2017, DOI: [10.1109/JESTPE.2016.2642831](https://doi.org/10.1109/JESTPE.2016.2642831).
- [4] G. Brando, A. Danner, A. D. Pizzo, R. Rizzo, and I. Spina, "Torque derivative control in induction motor drives supplied by multilevel inverters," *IET Power Electron.*, vol. 9, no. 11, pp. 2249–2261, 2016, DOI: [10.1049/iet-pel.2014.0958](https://doi.org/10.1049/iet-pel.2014.0958).
- [5] D. Zhou, J. Zhao, and Y. Li, "Model-predictive control scheme of five-leg AC-DC-AC converter-fed induction motor drive," *IEEE Trans. Ind. Electron.*, vol. 63, no. 7, pp. 4517–4526, Jul. 2016, DOI: [10.1109/TIE.2016.2541618](https://doi.org/10.1109/TIE.2016.2541618).
- [6] S. Du, B. Wu, N. R. Zargari, and Z. Cheng, "A flying-capacitor modular multilevel converter for medium-voltage motor drive," *IEEE Trans. Power Electron.*, vol. 32, no. 3, pp. 2081–2089, Mar. 2017, DOI: [10.1109/TPEL.2016.2565510](https://doi.org/10.1109/TPEL.2016.2565510).
- [7] N. Thitichaiworakorn, M. Hagiwara, and H. Akagi, "A medium-voltage large wind turbine generation system using an ac/ac modular multilevel cascade converter," *IEEE J. Emerg. Sel. Topics Power Electron.*, vol. 4, no. 2, pp. 534–546, Jun. 2016, DOI: [10.1109/JESTPE.2015.2462119](https://doi.org/10.1109/JESTPE.2015.2462119).
- [8] C. D. Fuentes, C. A. Rojas, H. Renaudineau, S. Kouro, M. A. Perez, and T. Meynard, "Experimental validation of a single dc bus cascaded h-bridge multilevel inverter for multistring photovoltaic systems," *IEEE Trans. Ind. Electron.*, vol. 64, no. 2, pp. 930–934, Feb. 2017, DOI: [10.1109/TIE.2016.2619661](https://doi.org/10.1109/TIE.2016.2619661).
- [9] P. Cossutta, M. P. Aguirre, A. Cao, S. Raffo, and M. I. Valla, "Single-stage fuel cell to grid interface with multilevel current-source inverters," *IEEE Trans. Ind. Electron.*, vol. 62, no. 8, pp. 5256–5264, Aug. 2015, DOI: [10.1109/TIE.2015.2434800](https://doi.org/10.1109/TIE.2015.2434800).
- [10] M. Quraan, P. Tricoli, S. D'Arco, and L. Piegaro, "Efficiency assessment of modular multilevel converters for battery electric vehicles," *IEEE Trans. Power Electron.*, vol. 32, no. 3, pp. 2041–2051, Mar. 2017, DOI: [10.1109/TPEL.2016.2557579](https://doi.org/10.1109/TPEL.2016.2557579).
- [11] D. Drews, R. Cuzner, and G. Venkataraman, "Operation of current source inverters in discontinuous conduction mode," *IEEE Trans. Ind. Appl.*, vol. 52, no. 6, pp. 4865–4877, Nov. 2016, DOI: [10.1109/TIA.2016.2590466](https://doi.org/10.1109/TIA.2016.2590466).
- [12] K. G. Sambandam, A. K. Rathore, A. Edpuganti, and D. Srinivasan, "Current-fed multilevel Converters: An overview of circuit topologies and modulation techniques," in *Proc. IEEE Ind. Appl. Soc. Annu. Meeting*, Oct. 2016, pp. 1–10, DOI: [10.1109/IAS.2016.7731887](https://doi.org/10.1109/IAS.2016.7731887).
- [13] Q. Wang, M. Cheng, and Y. Jiang, "Harmonics suppression for critical loads using electric springs with current-source inverters," *IEEE J. Emerg. Sel. Topics Power Electron.*, vol. 4, no. 4, pp. 1362–1369, Dec. 2016, DOI: [10.1109/JESTPE.2016.2591942](https://doi.org/10.1109/JESTPE.2016.2591942).
- [14] R. Ramachandran and M. Nyman, "Experimental demonstration of a 98.8% efficient isolated dc-dc GaN Converter," *IEEE Trans. Ind. Electron.*, 2016, to be published, DOI: [10.1109/TIE.2016.2613930](https://doi.org/10.1109/TIE.2016.2613930).
- [15] K. Armstrong, S. Das, and J. Cresko, "Wide bandgap semiconductor opportunities in power electronics," in *Proc. 4th Annu. IEEE Workshop Wide Bandgap Power Devices Appl.*, 2016, pp. 259–264, DOI: [10.1109/MPEL.2016.2557258](https://doi.org/10.1109/MPEL.2016.2557258).
- [16] D. Johannesson, M. Nawaz, K. Jacobs, S. Norrga, and H.-P. Nee, "Potential of ultra-high voltage silicon carbide semiconductor devices," in *Proc. 4th Annu. IEEE Workshop Wide Bandgap Power Devices Appl.*, 2016, pp. 253–258, DOI: [10.1109/MPEL.2016.2557258](https://doi.org/10.1109/MPEL.2016.2557258).
- [17] M. Aguirre, L. Calviño, and M. Valla, "Multilevel current-source inverter with FPGA control," *IEEE Trans. Ind. Electron.*, vol. 60, no. 1, pp. 3–10, Jan. 2013, DOI: [10.1109/TIE.2012.2185014](https://doi.org/10.1109/TIE.2012.2185014).
- [18] M. Huang, J. Zou, and X. Ma, "An improved phase-shifted carrier modulation for modular multilevel converter to suppress the influence of fluctuation of capacitor voltage," *IEEE Trans. Power Electron.*, vol. 31, no. 10, pp. 7404–7416, Oct. 2016, DOI: [10.1109/TPEL.2016.2514409](https://doi.org/10.1109/TPEL.2016.2514409).
- [19] J. Ebrahimi and H. Karshenas, "A new reduced-component hybrid flying capacitor multicell converter," *IEEE Trans. Ind. Electron.*, vol. 64, no. 2, pp. 912–921, Feb. 2017, DOI: [10.1109/TIE.2016.2618876](https://doi.org/10.1109/TIE.2016.2618876).
- [20] Y. Okazaki, H. Matsui, M. Muñoz, M. Hagiwara, and H. Akagi, "Enhancement on capacitor-voltage-balancing capability of a modular multilevel cascade inverter for medium-voltage synchronous-motor drives," in *Proc. IEEE Energy Convers. Congr. Expo.*, Sep. 2015, pp. 6352–6359, DOI: [10.1109/ECCE.2015.7310550](https://doi.org/10.1109/ECCE.2015.7310550).
- [21] P. Raj, A. Maswood, G. Ooi, and Z. Lim, "Voltage balancing technique in a space vector modulated 5-level multiple-pole multilevel diode clamped inverter," *IET Power Electron.*, vol. 8, no. 7, pp. 1263–1272, 2015, DOI: [10.1049/iet-pel.2014.0747](https://doi.org/10.1049/iet-pel.2014.0747).
- [22] Y. Okazaki, H. Matsui, M. Muñoz, M. Hagiwara, and H. Akagi, "Capacitor-voltage balancing for a modular multilevel DSCL inverter driving a medium-voltage synchronous motor," *IEEE Trans. Ind. Appl.*, vol. 52, no. 5, pp. 4074–4083, Sep. 2016, DOI: [10.1109/TIA.2016.2558638](https://doi.org/10.1109/TIA.2016.2558638).
- [23] Y. Li, E. A. Jones, and F. Wang, "The impact of voltage-balancing control on switching frequency of the modular multilevel converter," *IEEE Trans. Power Electron.*, vol. 31, no. 4, pp. 2829–2839, Apr. 2016, DOI: [10.1109/TPEL.2015.2448713](https://doi.org/10.1109/TPEL.2015.2448713).
- [24] A. R. S. S. Pramanick, M. Boby, K. Gopakumar, and L. G. Franquelo, "Extended linear modulation operation of a common-mode-voltage-eliminated cascaded multilevel inverter with a single DC supply," *IEEE Trans. Ind. Electron.*, vol. 63, no. 12, pp. 7372–7380, Dec. 2016, DOI: [10.1109/TIE.2016.2586441](https://doi.org/10.1109/TIE.2016.2586441).
- [25] N. Binesh and B. Wu, "5-level parallel current source inverter for high power application with dc current balance control," in *Proc. IEEE Int. Electr. Mach. Drives Conf.*, May 2011, pp. 504–509, DOI: [10.1109/IEMDC.2011.5994649](https://doi.org/10.1109/IEMDC.2011.5994649).
- [26] J. Bao, W. Bao, Z. Zhang, and W. Fang, "A simple current-balancing method for a three-phase 5-level current-source inverter," in *Proc. 35th Annu. Conf. IEEE Ind. Electron.*, Nov. 2009, pp. 104–108, DOI: [10.1109/IECON.2009.5414790](https://doi.org/10.1109/IECON.2009.5414790).
- [27] N. F. N. Ismail, N. A. Rahim, S. R. S. Raihan, and Y. Al-Turki, "Parallel inductor multilevel current source inverter with energy-recovery scheme for inductor currents balancing," *IET Power Electron.*, vol. 9, no. 11, pp. 2298–2304, 2016, DOI: [10.1049/iet-pel.2015.0909](https://doi.org/10.1049/iet-pel.2015.0909).
- [28] M. Aguirre, M. Engelhardt, J. Bracco, and M. Valla, "Current balance control in a multilevel current source inverter," in *Proc. IEEE Int. Conf. Ind. Technol.*, Feb. 2013, pp. 1567–1572, DOI: [10.1109/ICIT.2013.6505906](https://doi.org/10.1109/ICIT.2013.6505906).
- [29] A. Martins, V. Morais, M. Ferreira, and A. Carvalho, "Control architecture based on FPGA for a renewable energy system," in *Proc. 42nd Annu. Conf. IEEE Ind. Electron. Soc.*, Oct. 2016, pp. 4048–4053, DOI: [10.1109/IECON.2016.7793902](https://doi.org/10.1109/IECON.2016.7793902).
- [30] A. Cardenes, K. Agbossou, and N. Henao, "Development of power interface with FPGA-based adaptive control for PEM-FC system," *IEEE Trans. Energy Convers.*, vol. 30, no. 1, pp. 296–306, Mar. 2015, DOI: [10.1109/TEC.2014.2349653](https://doi.org/10.1109/TEC.2014.2349653).
- [31] M. Merai, M. W. Naouar, I. Slama-Belkhodja, and E. Monmasson, "FPGA-based fault-tolerant space vector-hysteresis current control for three-phase grid-connected converter," *IEEE Trans. Ind. Electron.*, vol. 63, no. 11, pp. 7008–7017, Nov. 2016, DOI: [10.1109/TIE.2016.2581758](https://doi.org/10.1109/TIE.2016.2581758).
- [32] G. A. Matig-a, M. R. Yuce, and J. M. Redouté, "An integrated LVDS transmitter-receiver system with increased self-immunity to EMI in 0.18- μ m CMOS," *IEEE Trans. Electromagn. Compat.*, vol. 58, no. 1, pp. 231–240, Feb. 2016, DOI: [10.1109/TEMC.2015.2505005](https://doi.org/10.1109/TEMC.2015.2505005).



Pablo Cossutta (M'12) received the Electronics Engineer (Hons.) and Specialist on Medical Equipment degrees from the Instituto Tecnológico de Buenos Aires (ITBA), Buenos Aires, Argentina, in 2001 and 2004, respectively, where he is currently working toward the Ph.D. degree in power electronics.

He is also an Associate Professor at ITBA, where he is involved in teaching and research on power and industrial electronics.



Miguel Pablo Aguirre (M'10–SM'16) received the Electronics Engineer degree from the Instituto Tecnológico de Buenos Aires (ITBA), Buenos Aires, Argentina, in 1995, and the Ph.D. degree from the Universidad Nacional de La Plata, La Plata, Argentina, in 2013.

He is currently the Head of the Department of Electrical and Electronics Engineering, ITBA, where he is involved in teaching and research on power electronics, power quality, and renewable energies as a Full Professor.



Mathias Angelico Engelhardt (M'12) received the Electronic Engineer (Hons.) degree from the Instituto Tecnológico de Buenos Aires (ITBA), Buenos Aires, Argentina, in 2014.

He is currently a Project Engineer with the Research and Development Center on Industrial Electronics, ITBA, where he does research with power and industrial electronics and its interfaces. He is also an Assistant Professor at ITBA.



María Inés Valla (S'79–M'80–SM'97–F'10) received the Electronics Engineer and Doctor in Engineering degrees from the National University of La Plata (UNLP), La Plata, Argentina, in 1980 and 1994, respectively.

She is currently a Full Professor with the Department of Electrical Engineering, Engineering Faculty, UNLP. She is also with the Consejo Nacional de Investigaciones Científicas y Técnicas, Buenos Aires, Argentina. She is involved in teaching and research on power converters, power quality, and renewable energies.

Dr. Valla is a co-Editor-in-Chief of the IEEE TRANSACTIONS ON INDUSTRIAL ELECTRONICS and a member of the IEEE James H. Mulligan, Jr. Education Medal Committee. She is also a member of the Buenos Aires Academy of Engineering in Argentina.